Mapping human cerebral blood flow with high-density, multi-channel speckle contrast optical spectroscopy

Byungchan (Kenny) Kim[1†], Alexander C. Howard[1†], Tom Y. Cheng[1,2], Jessica E. Anderson[1], Bernhard B. Zimmermann[1], Eric Hazen[1], Laura Carlton[1], Mitchell Robinson[2], Marco Renna[2], Meryem A. Yucel[1], Stefan A. Carp[2], Maria Angela Franceschini[2], David A. Boas[1], Xiaojun Cheng[1*]

[1]Neurophotonics Center, Department of Biomedical Engineering, Boston University, Boston, MA 02215, USA.
[2]Optics at Martinos Center, Massachusetts General Hospital and Harvard Medical School, Charlestown, Massachusetts 02129, USA.
[†] These authors contributed equally to this work.
*xcheng17@bu.edu

Abstract
Cerebral blood flow (CBF) dysregulation is correlated with pathologies including ischemic stroke and Alzheimer's disease. Portable real-time CBF monitoring, with spatial specificity, would aid neuroscience research and clinical decision-making. Recently, speckle contrast optical spectroscopy (SCOS) enabled non-invasive human CBF measurement, demonstrating a higher signal-to-noise ratio (SNR) compared to traditional optical methods. This work advances the SCOS state-of-the-art by developing a high-density, multi-channel SCOS system to map CBF during human brain activation. A laser multiplexed to 7 source fibers transmits light through multiple head locations to 17 cameras. Speckle images were analyzed to obtain optical density changes (ΔOD) based on tissue absorption, and relative CBF changes from laser speckle statistics. We validated the system's spatial specificity using a liquid phantom setup and demonstrated its application in measuring human brain activation maps, showing CBF and OD changes in the prefrontal cortex during a cognitive task. This work provides a tool for spatiotemporal monitoring of CBF for both neuroscience and brain health applications.

MAIN TEXT

Introduction
Cerebral blood flow (CBF) is a critical hemodynamic parameter that reflects the delivery of oxygen and nutrients to brain tissue, supporting neuronal function and brain health. Through neurovascular coupling, changes in CBF serve as indicators of brain functional activation [1,2]. CBF is also an important metric of brain health, as abnormal changes in CBF have been associated with numerous pathologies, including ischemic stroke [3,4], traumatic brain injury [5], Alzheimer's disease [6,7], and Parkinson's disease [8]. As such, monitoring CBF in clinical settings provides valuable information needed for diagnosis and clinical decision making. Many methods have been developed to monitor CBF, but are unsuitable for cognitive studies or clinical monitoring. For instance, magnetic resonance imaging (MRI) based arterial spin labeling is the current state-of-the-art method for CBF mapping, but it suffers from low signal-to-noise ratio (SNR), low temporal resolution, and high-cost from the need for high magnetic fields and dedicated, electrically-shielded imaging suites [9–11]. Similarly, computed tomography (CT) perfusion and 15O2 positron emission tomography also require expensive scanning hardware and, furthermore, involve ionizing radiation [12]. Thus, none of these existing high-end medical imaging methods are feasible for CBF

monitoring at the bedside or in naturalistic settings. Transcranial Doppler ultrasound is another method able to infer CBF from velocity measurements in large cerebral arteries, but is also relatively cumbersome, requires expert operators, and does not provide spatial maps of blood flow [13].

Optical methods enable development of low-cost, wearable systems that allow for continuous monitoring of the human brain at the bedside or in outdoor environments for naturalistic neuroscience studies. Diffuse correlation spectroscopy (DCS) is an optical method that captures flow information from the temporal dynamics of speckle patterns created by the interference of coherent light that scatters through the brain [14]. In DCS, the temporal speckle intensity autocorrelation function $g_2(\tau) = \langle I(t)I(t+\tau)\rangle / \langle I(t)\rangle^2$ is calculated and CBF is directly related to the apparent diffusion coefficient of scatterer mean square displacement that determines the shape of the $g_2(\tau)$ curve [15,16]. It is non-invasive, convenient to use, and has been applied in numerous clinical studies [17–19]. However, traditional DCS suffers from low SNR due to the need to sample individual speckles. DCS is therefore limited to relatively small source-detector separations (≤25 mm), where the sensitivity to the brain is low, i.e., the signal is more sensitive to the extracerebral (scalp and skull) rather than cerebral blood flow changes. Traditional DCS also utilizes relatively high-cost single photon avalanche diodes as detectors, making it expensive for DCS to scale to a multi-channel system capable of covering a large area of the brain, or averaging over multiple speckles to improve SNR. Interferometry has been shown to improve DCS SNR [20,21], but at the expense of increased system complexity which is not preferred for the development of multi-channel or wearable devices.

Speckle contrast optical spectroscopy (SCOS) is another optical technique that is capable of measuring CBF, which has grown rapidly over the last few years showing competitive advantages over DCS [22–28]. Instead of directly measuring the speckle dynamics as done in DCS, SCOS calculates the contrast of the speckle pattern over space or time, defined as the ratio between the standard deviation and the mean of the intensities of the speckle images, $K = \frac{std(I)}{\langle I \rangle}$. SCOS can achieve higher SNR than DCS (>10x), thanks to the averaging of the contrast over thousands to millions of pixels/speckles available with low-cost complementary metal-oxide semiconductor (CMOS) cameras [29]. Recently, we presented the ability of single-channel SCOS to measure changes in CBF through computational modeling [30] and experimental validations using a scientific CMOS (sCMOS) camera [25]. We then found that more affordable, commercial CMOS cameras can also be used for SCOS measurements and can achieve accurate measurements comparable to those measured with costly sCMOS cameras [31]. These more affordable detectors make it feasible and accessible to build a multi-channel system to cover a large area with multiple sources and detectors. The resulting overlapping source-detector pairs have photon trajectories that cover different parts of the brain, allowing for spatially specific measurements of CBF changes in the brain.

In this manuscript, we present the development of a multi-channel, high-density SCOS system consisting of 7 sources and 17 detectors that can map CBF changes over an area of 7.6 cm by 6.6 cm with a high measurement density (19 mm nearest neighbor source detector separation (SDS), excluding short separation channel). While numerical simulations have suggested the potential of SCOS for tomographic brain imaging [32], and preliminary studies have demonstrated its ability to measure cerebral blood flow in humans at a single channel [25,33], robust mapping of human brain function with high-density SCOS systems has not yet been achieved. We have temporally

multiplexed 7 source positions at 14.3 Hz, sufficient to appropriately sample task-induced hemodynamic responses. We demonstrated the spatial specificity of the high-density measurements using a flow phantom that produced a local change in flow velocity. We then conducted human brain function measurements using a word-color Stroop (WCS) task [34]. The results show the capability of our multi-channel, high-density SCOS system to non-invasively map changes in CBF in the human brain, providing a valuable tool for studying hemodynamic responses and brain function in diverse cognitive and clinical applications.

Results

The schematic of the multi-channel SCOS system consisting of 7 sources and 17 detectors is shown in Fig. 1a. For the source, we used a volume holographic grating (VHG) laser (Thorlabs LD852-SEV600, 850 nm). The laser was collimated, isolated, steered with two galvanometer mirrors, and focused with an achromatic lens onto seven different multi-mode fibers in an MTP fiber array. The multi-mode fibers transmitted the laser light to different locations on the head. Using a 6.2 mm focal length collimation lens and a 50 mm focal length achromatic focusing lens, we achieved a focal spot of 41x48 µm full-width at half-maximum (Fig. S1a, 1b). This coupled most of the light into the multi-mode source fiber (~80%). The distal end of each source fiber was placed in a 3D-printed fiber holder and coupled to a mirror angled at 45° and an acrylic light pipe that directed the light towards the skin (Fig. 1b). The 16 detectors consisted of a bundle of multi-mode fibers that transmitted the speckle patterns formed by reemitted photons on the head to a camera, with two plano-convex lenses (NA = 0.79 $f_1 = 16$ mm; NA = 0.36, $f_2 = 35$ mm) creating a 4f system to magnify the image (2.2x). The plano-convex lens closer to the fiber bundle was moved slightly off-focus (2-3 mm) to reduce spatial variance from illumination heterogeneity of each individual fiber in the bundle (Fig. S1c). With slight defocusing, the resulting speckle-to-pixel size ratio (s/p) was between 0.75 and 0.87 (Table S1). This was characterized from static phantom speckle contrast measurements for each individual detector. For short separation, the 17th detector had a NIRx short channel coupled to a 1 mm diameter SMA optical fiber (0.22 NA). This fiber was then connected to the camera sensor, positioned 15 mm away from the fiber tip. The optodes were placed in a hexagonal grid with the nearest source-detector separation (SDS), excluding the separate short separation channel, at 19 mm, followed by the second nearest SDS at 33 mm (Fig. 1c,d). The short separation NIRx channel was placed adjacent to source 7 at 8 mm SDS. The diagram of the control system for the multi-channel SCOS set-up is shown in Fig. 1e. More details on the system setup are provided in the methods section.

We evaluated the stability of our system's laser light inputs and tested the temporal multiplexing needed to illuminate multiple source positions with a single laser light source. To test the optical stability of the system during light steering, we mounted the SCOS system onto a static phantom at 15 mm SDS. The detector fiber mounted camera captured images with 4 ms exposure time at 14.3 Hz, while two different voltage patterns were provided to the galvanometers. The voltage applied to the two galvanometers controls the mirrors' positions, allowing precise manipulation of the beam direction along two dimensions. We recorded the mean intensity of the images captured by the camera, both with constant voltage given to the galvanometers and with a trapezoidal waveform galvanometer voltage input consisting of upslope, plateau, downslope, and trough durations of 1.0, 5.2, 1.0, and 2.8 ms, respectively. We used a trapezoidal instead of a rectangular waveform to reduce galvanometer mirror vibration caused by acceleration. The camera frame start triggers were synchronized to 1.0 ms after beginning of the plateau. This same trapezoidal waveform pattern is used in all subsequent multi-channel SCOS measurements. Example mean

intensity time courses from both galvanometer voltage input patterns is shown in Fig. 2a. We measured the drift in normalized intensity after 30 seconds as to have standard deviation of 3.9×10^{-4} (N = 20) when the galvanometer mirrors remain stationary versus 4.9×10^{-4} (N = 20) when the galvanometer mirrors move between source fibers. 30 seconds was chosen as a conservative expected time needed to see cerebral activation induced change in intensity. This variation is significantly smaller than the expected intensity signal changes of 1×10^{-2} to 2×10^{-2} during brain activation. In Fig. 2c, we show a baseline phantom measurement using a liquid phantom (intralipid 1.6% v/v in deionized water at room temperature) with camera exposure time of 4 ms. Fig. 2c shows the average intensity recorded by each detector camera when light was launched sequentially through all the source locations. The intensity level is related to the source-detector separations, showing that the temporal multiplexing scheme is working as expected. For instance, at detector #1, the closest light source is source #1, followed by source #3. As expected, the intensity is highest when source #1 is illuminated and second highest when source #3 is illuminated.

Next, we tested our system's ability to capture cardiac waveforms from the human head. The source-detector array was placed on the human forehead as shown in Fig. 3a. We show the time courses of $\Delta OD = -\ln\left(I/I_0\right)$, where I_0 is the mean intensity over the measurement period, and relative blood flow index (BFi) $= 1/K_f^2$ for 12 of the channels with SDS of 33 mm in Fig. 3b. We can clearly visualize the cardiac waveforms simultaneously in all the channels for both ΔOD and BFi. Magnitude and waveform shape of both ΔOD and BFi were different between channels.

To demonstrate our system's capability to localize flow variations, we used a dynamic phantom sample (intralipid 1.6% v/v) placed in an acrylic tank with a transparent, thin-walled tube (0.082 inches inner diameter) positioned 12 mm from the tube center to the fiber tips of the high-density probe. The tube was subjected to bulk flow at 2 cm/s for 30 s, followed by 30 seconds of no flow to allow baseline recovery. This cycle was repeated 6 times, with the time course of the flow shown in Fig. 4a. The time courses of the changes in relative BFi and ΔOD from -10 to 45 seconds (with 0 second indicating the onset of the flow) are shown in Fig. 4c and d respectively. These averages, taken over 6 blocks, are displayed in channel space for SDSs of 19 mm and 33 mm, and for the orientations of the source-detector layout relative to the tube (0°, 45°, 90°) as illustrated in Fig. 4b. The profiles were obtained using the plot probe function in Homer3 [35]. We observe that the relative BFi increases from 0 to 30 seconds for channels (i.e. source-detector pairs) overlying the tube, while no change is seen in ΔOD, as expected, since there were no absorption changes. This illustrates that our multi-channel, high-density SCOS system can measure spatiotemporal BFi changes, which is an independent parameter not accessible with fNIRS, which only measures ΔOD as a reflection of blood volume or concentration changes. Additionally, we see that the amplitude of "activation" across channels varies with different orientations of the source-detector layout, with channels spatially closer to the tubes consistently showing larger BFi changes. This highlights the varying sensitivity of SDS channels to localized flow changes.

Finally, we conducted human brain function measurements using a WCS task (Figs. 5a,b) consisting of a congruent and an incongruent task condition, as described in the Methods section. In congruent trials, the participant chooses the word with matching color and meaning. In incongruent trials, the participant chooses the word in the top row with meaning matching the color of the word in the bottom row. The WCS task was selected for this study due to two key

advantages. First, the task activates the prefrontal cortex, which is in a hair-sparse region of the head, enabling optimal optode placement without compromising photon flux. Second, it allows for measurement of participant engagement through feedback on task accuracy. Out of the 19 participants measured, data from 15 participants, which had more than half of the blocks not contaminated by motion artifacts, were further analyzed. The participants overall showed high task performance, with average answer accuracy of 96.6% (standard deviation of 4.87%, range from 82% to 100%). When divided into congruent and incongruent task performance, participants chose the correct answer 99.5% (standard deviation = 1.12%) for congruent tasks and 93.9% (standard deviation = 9.52%) for incongruent tasks. The collected images were preprocessed to obtain windowed mean and variance, then the preprocessed data is analyzed to obtain both ΔOD and rBFi. We linearly regressed out the short separation channel from both signals, thereby obtaining ΔOD with smaller scalp contribution, and relative CBF (rCBF). Change in relative CBF (ΔrCBF) is simply rCBF subtracted by baseline of 1. ΔrCBF was then low pass filtered (0.2 Hz) and averaged over blocks and participants to obtain activation time courses over channel space for 15 participants (Figs. 5c,d). For each signal type (ΔOD, ΔrCBF), significant channels were found as those with mean activation at $t > 10s$ and $t < 15s$ greater than 1.96 times standard error. The spatial distribution of the significant channels for ΔOD covered both lateral and medial regions, while the significant channels for ΔrCBF covered only the lateral regions, with six 33 mm SDS channels overlapping between the two signal types. The average ΔOD activation of those channels under incongruent task was 0.00420 ± 0.00177 ($p = 0.0176$, $n = 15$) for 19 mm SDS and 0.00803 ± 0.00310 ($p = 0.0096$, $n = 15$) for 33 mm SDS while the average ΔrBFi activation of those channels under incongruent task was 3.27 ± 1.16% ($p = 0.0048$, $n = 15$) for 19 mm SDS and 3.53 ± 1.24% ($p = 0.0044$, $n = 15$) for 33 mm SDS. The same channels did not have significant activation with congruent tasks.

We utilized a Monte Carlo model integrated with cedalion, a Python fNIRS analysis toolbox, to reconstruct both the ΔOD and ΔrCBF images (Figs. 5 e-j) [36]. The sensitivity matrices for ΔOD (Fig. 5 e) and ΔrCBF (Fig. 5 h) are shown as a sum of the sensitivity across channels. Both show higher sensitivity to superficial gyri within the region encompassed by the optodes. The congruent task (Fig. 5 f,i) shows little to no activation in both ΔOD and ΔrCBF. The incongruent task (Fig. 5 g,j) shows broad activation in the lateral region of the cortex, congruent with prior Stroop task literature [37].

Discussion

Our multi-channel SCOS system demonstrates robust capabilities for CBF monitoring with high spatial specificity and temporal resolution, marking a significant advancement in the field. We expanded on our prior work with a one-source, one-detector SCOS system by using a galvanometer to illuminate 7 source fibers, increasing the number of inexpensive commercial CMOS cameras, and validating the source illumination stability and temporal multiplexing. We demonstrated the multi-channel SCOS system's ability to measure physiological signals, as well as its spatial specificity to underlying flow change with a dynamic phantom experiment. The human applicability of the system was presented by noninvasively measuring spatially specific WCS task-induced CBF changes in humans.

Measurement of clear cardiac waveforms in a dozen 33 mm SDS channels shows the value of the SNR and the temporal resolution of the multi-channel SCOS system compared with alternatives. The BFi waveform is sharper than the ΔOD waveform for most channels, in line with prior

literature reporting measurement of both waveforms on the upper limb [38,39]. Cardiac blood flow waveforms in the human brain have previously been non-invasively measured using DCS [40,41]. However, the approach required cardiac-gated averaging of several pulse cycles, and was difficult to implement for large number of channels due to the prohibitive cost of SPADs and correlators. With multi-channel SCOS, we can start investigating the spatial heterogeneity of blood flow changes, in relation to both systemic physiology and cognitive activation.

For the liquid phantom experiment, we chose 12 mm tube depth from fiber tip to match the distance of the brain from the scalp on the forehead [42]. We measured underlying flow with the multi-channel SCOS system at different tube orientations (0°, 45°, 90°) and showed that different channels have higher rBFi, in line with the expectation. For example, channels that spatially do not overlap with the tube at 0° but do at 90° (S3D5, S3D11) show rBFi increase only with the tube at 90° orientation. The magnitude of rBFi increase was in general larger for 33 mm SDS channels than 19 mm SDS channels, consistent with the higher sensitivity of the larger SDS channels to deeper flow change. One limitation of this experiment is that flow through the tube primarily increases convective flow, rather than diffusive flow. Meanwhile, prior Monte Carlo simulation of DCS showed primary contribution from diffusive flow in biological tissue [43], meaning there is a mismatch in the cause of rBFi increase between phantom and *in vivo* measurement.

Prior human studies measuring cognitively activated cerebral blood flow change used visual stimuli and motor task. We chose WCS task because it activates the prefrontal cortex which is in a hair-sparse region of the head, allowing for easier optode placement without compromising photon flux, and because participant engagement can be measured through their task accuracy.

The sensitivity matrices used for image reconstruction on the human brain look generally similar between ΔOD and ΔrCBF. This is expected, as photons are traveling through the same region for both measurements. Slight differences can be attributed to the difference between the effect of absorption perturbation on intensity and a blood flow perturbation on the autocorrelation, and thus K_f^2 [23].

Our human measurements show statistically significant channels distributed differently for ΔOD and ΔrCBF. While significant ΔOD channels are present both medially and laterally, significant ΔrCBF channels are only located laterally. The same pattern is seen in the reconstructed image, where the ΔOD map shows broader activation pattern than ΔrCBF. One possible reason for different distribution between ΔOD and ΔrCBF is that the ΔOD medial increase is not due to increased neural activity leading to vasodilation, but rather decreased neural activity increasing the ratio of oxyhemoglobin (HbO) to deoxyhemoglobin (HbR). Since the laser is approximately 1.5x more absorptive to HbO than HbR, this reason would explain the increased ΔOD and the stable ΔrBFi. Another possibility is that ΔrBFi has lower contrast-to-noise ratio (CNR), where either low change in signal or high noise makes it difficult to see medial change in ΔrCBF.

Several technical considerations and limitations merit discussion. One practical challenge is the variation in coupling efficiency between source fibers, leading to differences in light intensity among the seven sources (approximately 20%). While this variation affects the signal-to-noise ratio across different channels, it does not impact the mean values of OD and rCBF. This is because both the numerator and denominator of $e^{\Delta OD}$ are linearly proportional to intensity, and rCBF remains intensity-invariant if noise correction is properly applied.

The temporal resolution of our system is currently constrained by the multiplexing strategy employed. Each source position requires 10 ms using trapezoidal waveforms to control the galvanometer mirrors, resulting in a maximum frame rate of 14.3 Hz to cycle through all seven sources. Although this resolution is sufficient for capturing the hemodynamic responses relevant to our study and cardiac waveforms, future systems with more channels may need multiple laser sources operating in parallel to maintain adequate temporal resolution for other applications.

Regarding spatial resolution, our current setup covers a 7.6 cm x 6.6 cm area with source-detector separations (SDS) ranging from 19 mm to 33 mm. The spatial resolution of this multi-channel SCOS system is expected to be comparable to that of fNIRS with a similar optode density [44], though coarser than traditional neuroimaging methods like fMRI. This limitation arises from the number of channels that cover different parts of the brain. Increasing the optode density in the future could improve the spatial resolution [45].

Motion sensitivity is another challenge, as observed in most optical imaging techniques. Head motion affects the optode-to-head coupling, resulting in signal artifacts [46]. While we minimized head motion during our human participant measurements using a chin mount and instructions to the participants, we still observed significant intensity fluctuations in more than half of the blocks in four of the 19 participants, leading to their data being excluded. A potential solution could involve a fiber-free SCOS system, allowing for more naturalistic behavior and expanding the scope of neuroscience and clinical applications [33].

Furthermore, the current implementation requires careful positioning of the optodes to ensure good coupling with the scalp and proper threading through hair. Although we have optimized the fiber holders and mounting system with spring tops, maintaining consistent coupling during long measurement sessions remains a practical challenge that needs to be addressed in experimental design.

The SCOS system uses 17 cameras, each with 2 million pixels and 16 bits per pixel, capturing data at 100 frames per second over 14 minutes. This setup generates approximately 12 terabytes of data per participant. Measurement duration is therefore limited by the available computer storage. Our preprocessing pipeline, which calculates the windowed mean and variance for each image and deletes the raw speckle images, reduces the data size to hundreds of gigabytes. However, this process is currently implemented post hoc. A real-time implementation of preprocessing would enable significantly longer measurement time; however, extensive validation is needed to ensure that the proper noise correction is maintained during real-time image processing.

Another confounding factor is the potential for participants to develop increasing familiarity within the task over the course of the experiment, which may influence the hemodynamic response. Additionally, participants often reported feeling increasingly tired as the experiment progresses, which could further impact the measurements. To characterize the potential confounds, the hemodynamic response was compared between the first and second run of the experiment. For the congruent task, larger activation was observed in run 1 for both ΔOD (0.00618±0.00363, $p = 0.0887$) and ΔrCBF (2.17±1.19%, $p = 0.0682$) than in run 2 (0.00165±0.00255, $p = 0.518$; -0.734±0.957%, $p = 0.443$), suggesting that repeated exposure made the task insufficiently challenging to induce activation (Fig. S2). For the incongruent task, significant activation was observed during both runs, with a greater magnitude during run 2 (Fig. S2). Incongruent task induced ΔOD was 0.00669±0.00342 ($p = 0.0504$) and 0.00900±0.00437 ($p = 0.0394$) for run 1 and

2 respectively. ΔrCBF was 3.31±1.13% (p = 0.0034) vs 3.71±2.07% (p = 0.0731) for the respective runs.

Looking ahead, this multi-channel SCOS system shows tremendous potential for advancing functional neuroimaging. Future work includes implementing real-time preprocessing algorithms to extend measurement durations and improve data management efficiently. Adding more channels for higher density could improve the spatial resolution, while whole head coverage would allow for further neuroimaging applications such as imaging of functional connectivity.

Potential research applications include mapping of cerebral activation in response to various stimuli (finger tapping, visual tasks), and comparing cerebral blood flow and cerebral blood volume based resting-state functional connectivity [47]. With further development, potential clinical research applications could include monitoring of cerebral hemodynamics under conditions of disrupted cerebral homeostasis, such as during anesthesia, acute neurological disorders like cerebral infarction, and chronic neurological disorders such as Parkinson's disease and Alzheimer's diseases [6,8].

Materials and Methods

Multi-channel fiber-based SCOS system

The schematic of our multi-channel fiber-based SCOS system is illustrated in Fig. 1. The input laser light source (Thorlabs LD852-SEV600; 852 nm) is first collimated using a planoconvex lens (Thorlabs C110TMD-B; NA = 0.4), then passed through an optical isolator (Thorlabs IO-5-850-VLP). The light then enters a galvanometer scanner (Thorlabs GVSK2-US) and is focused down using a planoconvex lens (Thorlabs AC254-050-B; NA = 0.25). The galvanometer couples the focused light into an MTP connectorized fiber bundle containing 12 multimode fibers (62.5 μm core diameter, 0.22 NA), 7 of which are coupled to acrylic light pipes of 3 mm diameter that deliver the light to a sample such as the human head. We utilized custom-made fiber bundles (~3770 strands of 37 μm core diameter multimode fiber, 0.66 NA) with circular shape on the proximal end (~2.5 mm diameter) to facilitate scalp contact through the hair and rectangular shape on the distal end (~1.64 × 3 mm) to match the rectangular shape of the CMOS sensors used as detectors. We imaged 16 bundles from different locations on the human scalp onto 16 CMOS (Basler a2A1920-160umPRO) cameras. The fiber bundle was imaged using a 4f system consisting of higher NA lens closer to the fiber (Thorlabs ACL25416U-B; NA = 0.79) followed by lower NA lens (Thorlabs LA1027-B, Edmund Optics 38-421; NA = 0.36) as shown in Fig 1a. The cameras operate at 10-bit resolution with 16 dB gain and a black level of 25 arbitrary digital units (ADU) resulting in an expected read noise of 2.1 e- across the sensor. We slightly defocus the imaged speckle to fill the gaps between individual fibers within a single fiber bundle as shown in Fig. S1, resulting in a reduction in spatial heterogeneity of the illumination on the sensor. The s/p for the system has been calibrated to be 0.7-0.8 from $K_f^2 = \beta = \frac{(s/p)^2}{2(1+(s/p)^2)}$ for unpolarized light obtained using a static phantom sample at high photon flux values to reduce errors introduced by noise [30]. The sources and detectors are arranged in a symmetrical hexagonal grid as shown in Fig. 1c. Additionally, a short separation channel is included using a commercial NIRx short-separation fiber holder module mounted around the source optode 7 to achieve an SDS of 8 mm for short separation regression [48]. The NIRx module contains a fiber bundle that is coupled to a 1 mm diameter multimode fiber that projects light directly onto a camera. Due to the smaller SDS, the amount of

light in the short-separation channel is significantly higher, allowing for direct projection into a 17th CMOS camera without requiring optimal detector coverage.

The source focal spot size was measured by reducing the laser diode current to 3.2 mA and placing the camera at the same z-plane as the fiber array. The laser diode had a maximum output power of 600 mW. The power achieved at the source fiber holder was approximately 270 mW. This reduction is attributed to ~80% transmission efficiency through the isolator, ~70% fiber coupling efficiency, and ~80% mirror and acrylic coupling efficiency. To meet with ANSI safety standards, each fiber is illuminated for 5.2 ms every 70 ms, resulting in a 7.4% duty cycle, which reduce the average power to 20 mW. This ensures both the peak and average power are within the ANSI safety limits.

The 7 source fibers and 17 detector fiber bundles are placed in a 76 mm by 66 mm rectangular grid (Fig 1c), resulting in 28 pairs of 19-mm SDS channels and 22 pairs of 33-mm SDS channels. For human measurements, the grid is placed on the right forehead to target the right lateral frontal lobe (Fig 1d).

Multiplexing scheme using galvanometer mirrors

Multiplexing of the sources is achieved using a galvanometer and a fiber array. As shown in Figure 1, the laser source is collimated then sent into the galvanometer which is controlled by an Arduino connected to an external digital to analog converter (DAC) using a custom designed printed circuit board (PCB). The two galvanometer mirrors, each rotating orthogonal to the other to achieve two-dimensional coverage, steers the light into one of the fibers, where a focusing lens focuses the collimated beam to a spot for improved coupling with the fibers. The beam is sequentially steered to sources 1 through 7, pausing at a safety fiber between each source (details on the safety fiber's purpose are provided below). Each fiber is routed to a unique location on the head, enabling multichannel measurements through temporal multiplexing.

To achieve optimal coupling, a galvanometer optimization protocol is conducted to locate the coordinates of each fiber. This is repeated before each measurement to minimize light losses. The protocol is controlled by an Arduino script. The Arduino receives input from a Thorlabs power meter (Thorlabs PM400) at which the source fiber is pointed to measure the amount of light from a given source fiber. First, the estimated coordinates are input to the Arduino. Then the galvanometer steers the beam in a spiral radiating outward from the starting coordinate until the threshold of approximately 1 mW is reached. Once the threshold is reached, the galvanometer steers the beam in a line approximately 20 µm in both directions from the starting coordinate. The X coordinate is then set to the peak value along the line scan. The process is repeated for the Y direction. This is repeated until there is no coordinate with higher intensity in either X or Y. Finally, for fine tuning, a square grid of about 40 by 40 µm centered at the highest intensity coordinate is generated, and the laser is scanned throughout the grid. The peak value in the grid is selected as the final coordinate for the source fiber in question. This process is repeated for all source fibers and the safety fiber, which takes approximately 10 minutes. The coordinates are then saved for later use for the measurements.

Time synchronization

Because brain activation is measured as an average of the blocks in the task, it is important to be able to synchronize the frames collected by the camera with the time the stimulus is given, which is measured using a National Instruments (NI) card. To achieve synchronization, the Arduino connected to the PCB acts as the primary device, and the cameras, galvanometer, and NI card act as secondary devices. On the first frame of the measurement, the Arduino directs the laser to the first source, by varying the voltage on the galvanometer, then immediately sends a pulse train at 100 Hz to the cameras. In this way, the first frame for each camera is coming from the first source, and all subsequent frames are synched because the pulse the Arduino sends to trigger frame acquisition is sent after the time the Arduino has steered the galvanometer angles to illuminate each successive source fiber.

A stimulus tracker (StimTracker Quad, AD Instruments) is connected to a photodiode that tracks the brightness of a corner of the screen that the participant views for the task. The corner of the screen is filled with a white rectangle when the stimulus is given and a black rectangle when there is no stimulus, providing the stimulus tracker with the time of the stimulus. An NI card receives the transistor-transistor logic signal from the stimulus tracker and Arduino's pulse train indicating frame start. This provides information on which frame the task starts for each block, allowing for block averaging.

Pulsing strategy to improve photon flux

We utilize a laser pulsing strategy to improve photon flux while staying within the ANSI laser tissue exposure limits. Before measurement begins, the galvanometer directs the laser onto an eighth fiber connected to a photodiode that controls a safety circuit. During measurement, every 10 ms, the galvanometer steers the light to this eighth fiber for 5.2 ms. If light does not reach the eighth fiber within the 10 ms interval, the safety circuit shuts off the laser to prevent any single fiber from illuminating the tissue for an excessive duration. Additionally, the temporal multiplexing ensures that a different source is illuminated during each 10 ms period, with the same source only being illuminated again after all the 7 sources have received illumination, thus achieving a duty cycle of 5.2 ms/ (7× 10 ms)=7.4% for each source. This enables a higher peak power to be sent to the head during acquisition while keeping a lower safe average power and ensures that both the average and peak power are within the ANSI safety limit.

Acquisition software

Camera frames are acquired using a python script employing the PyPylon module. The script performs parallel processing, acquiring frames from each camera simultaneously. It also performs multicore processing assigning 2 CPU cores to each camera. For each camera, the script collects frames and stores them in random access memory (RAM) until 1000 frames are accumulated, at which point they are saved simultaneously. The number of frames collected before saving is a trade-off: collecting too many frames risks exhausting the RAM and losing new incoming frames, while collecting too few frames results in frequent saving, which can delay processing and cause a buildup of frames in RAM, also leading to data loss. As such, a buffer size of 1000 frames was chosen as it avoids overloading the RAM, and minimizes the frequency of saving operation. It should be noted that while this process is not perfectly efficient, and may lead to a gradual buildup of frames in RAM, the rate is slow enough to avoid issues within the timeframe of our experimental design. However, this should be considered for longer measurements. We found that the required

data transfer rate could be sustained by saving data from two cameras to a single hard drive. Each computer utilized 4 hard drives to handle data from 8 cameras simultaneously. This setup required three computers: two for collecting data from the 16 cameras in the high-density patch, and a 3rd computer for managing the short separation camera and running the WCS cognitive task. At the end of each run, a timestamp file was saved, recording the acquisition time for each frame. This file is used during data analysis to identify and correct any potential lost frames.

Data analysis pipeline for multichannel fiber-based SCOS

Because of the immense size of the raw speckle images (approximately 12 TB per 7 min measurement), data analysis is very time-consuming. To manage this, the process is divided into 3 steps, with some analysis performed locally on the computer where the data is recorded, and the rest conducted on remote compute servers after pre-processing reduces storage requirements. The three steps are: preprocessing (calculating windowed mean and variance), analysis (calculating K_f^2), and post-analysis (filtering, regression, block averaging) [49].

The size of the data is large due to the high pixel count of each camera. Since only the mean intensity and spatial variance are needed from each frame to calculate intensity and contrast, each camera frame can, in principle, be reduced to these two values, significantly shrinking the data size. This is what is done during preprocessing. In practice, the process is more complex, because some noise corrections require unique value for each pixel. These corrections must be applied before calculating the mean and the spatial variance.

During preprocessing, the timestamp of each frame is first used to correct for any missed frames. Then, the source illumination is assigned for each frame. Next, the temporal mean dark image, obtained by recording frames with the laser off after each measurement, is subtracted from each camera frame to account for the contribution of dark counts. The windowed temporal variance of the dark images is also saved for later subtraction. After dark subtraction, the mean image is calculated as the temporal mean of all frames for a given source. Finally, pixels are grouped into 7x7 windows, and the mean and variance of each window are calculated. In the analysis, the windowed mean and variance are used to calculate the speckle contrast. To perform proper noise correction, the contrast squared from shot noise, read noise, quantization noise, and spatial heterogeneity are also calculated so they can be subtracted for each window as shown below in Eqs. 1-6.

$$K_{raw}^2 = \frac{\sigma_{window}^2}{<I_{window}>^2} \tag{1}$$

$$K_s^2 = \frac{g}{<I_{window}>} \tag{2}$$

$$K_r^2 = \frac{<\sigma_{dark,\,window}^2> - 1/12}{<I_{window}>^2} \tag{3}$$

$$K_q^2 = \frac{1/12}{<I_{window}>^2} \tag{4}$$

$$K_{sp}^2 = \frac{\sigma^2_{mean\ image}}{<I_{mean\ image}>^2} \tag{5}$$

$$K_f^2 = K_{raw}^2 - K_s^2 - K_r^2 - K_q^2 - K_{sp}^2 \tag{6}$$

Where K_{raw}^2 is the contrast squared from the raw dark subtracted data before noise correction, σ^2_{window} is the windowed variance, $<I_{window}>$ is the mean intensity of the window, K_s^2 is contrast squared from shot noise, g is the camera gain, K_r^2 is the contrast squared from read noise, $<\sigma^2_{dark,\ window}>$ is the spatial mean of the temporal variance of the dark image within a window, K_q^2 is the contrast squared from quantization noise, K_{sp}^2 is the contrast squared from spatial heterogeneity, $\sigma^2_{mean\ image}$ is the spatial variance of the temporal mean image, $<I_{mean\ image}>$ is the spatial mean intensity of the temporal mean image, and K_f^2 is the fundamental contrast squared due to dynamics in the scattering medium, which is of interest. The contrast terms are weighted by the intensity squared and normalized to provide higher weight to windows that received more photons as shown below in Eqs. 7 and 8.

$$w_{window} = \langle I_w \rangle^2 \Big/ \langle \langle I_w \rangle^2 \rangle \tag{7}$$

$$K^2_{f,image} = \langle w_{window} K^2_{f,window} \rangle \tag{8}$$

Blood flow index (BFi) is calculated as the inverse of the window averaged fundamental contrast squared (Eq. 9).

$$BFi = 1 \Big/ K^2_{f,image} \tag{9}$$

Camera characterization

Camera characterization is done to plot the photon transfer curve that enables the accurate subtraction of shot noise and read noise contributions from K^2_{all} [31]. A 785 nm LED is mounted to one port of an integration sphere, with a camera connected to the other port. To limit the range of angles of light incident on the detector surface, the camera is attached to a long lens tube (at least 30 cm in length). The LED is connected to a variable power supply, and the voltage to the LED is increased incrementally such that the light intensity recorded from the camera spans the full-scale range of the camera. In this way, the camera intensity variance for each intensity level can be quantified, thus constructing the photon transfer curve.

The entire process is automated using a python script. The script defines a logarithmic scale of intensity values that span the full dynamic range of the camera. The script is responsible for both

controlling the power supply and acquiring camera frames. It first acquires dark frames with zero voltage supplied to the LED to measure the dark noise. Then it increments the LED voltage by 1 mV. The intensity is then averaged across the entire frame, and, if the intensity threshold defined by the logarithmic scale is met, the software collects camera frames at that intensity. A logarithmic range is used because typical human measurements occur in the low photon count range, thus given a finite number of measurement points, it is more valuable to have a denser coverage at lower counts. Camera frames are acquired using the PyPylon module, and the power supply is controlled using the PySerial module.

Static phantom s/p measurements

Static phantom measurements were conducted to measure the s/p ratio for each camera. A static phantom mimicking human tissue optical properties (μ_a = 0.0188 mm-1, μ_s' = 0.0736 mm-1) was clamped to the optical table using optomechanical components for stabilization. Next, one of the fiber connector physical contact (FCPC) ends of the source fiber bundle was clamped to the phantom. A detector optode containing the detector fiber bundle was placed 19 mm away from the source fiber. The setup was tightened meticulously to ensure minimal motion to prevent decorrelation of the speckle pattern within the duration of the exposure time. This was verified by monitoring the speckle pattern in real time using the Pylon software and ensuring that any observed fluctuations were occurring on time scales slower than a few seconds. Once this was verified, 100 camera frames were recorded with exposure time of 20 μs using a current of 983 mA. From this data s/p ratio was calculated using a MATLAB script. First the fundamental contrast squared is calculated as described above in Eq. 1-6, except contrast squared from spatial heterogeneity is not subtracted, since for static phantom the temporal mean image is the same as the speckle pattern thus it does not provide an estimation of the non-homogeneity in the illumination. We have found that this contribution is three orders of magnitude smaller (K_{sp}^2 = 0.00010) e.g. compared to the K_f^2 for a static phantom (e.g. 0.191), thus its effect can be ignored. Then s/p ratio is estimated as $s/p = \sqrt{\frac{K_f^2/\beta_l}{1-K_f^2/\beta_l}}$. Here β_l is the coherence parameter of the source, which is assumed to be 0.5 because the light is coherent and unpolarized.

Liquid dynamic phantom measurements

The dynamic phantom consists of an acrylic container filled with 1.6% intralipid and a thin polytetrafluoroethylene tube (inner diameter = 0.082 inches, wall thickness = 0.005 inches) also containing the same intralipid solution. The tube is connected to a syringe pump that enables changing of the flow rate within the tube. The fibers are arranged in a grid with the same SDS as used in human measurements (Fig. 1). This grid is rotated at three angles, 0°, 45°, and 90° (Fig. 4), to demonstrate the system's ability to observe a localized increase in BFi. At each angle, 400 seconds of measurement is taken. There are 6 blocks each consisting of 30s no-flow followed by 30s flow, ending with 40s no-flow to allow the BFi time course to return to baseline as shown in Fig. 4a. A flow rate of 2 cm/s is used during the flow period to mimic biologically relevant flow changes. During no-flow, the syringe pump is turned off. To remove any temporal fluctuation (ΔOD or BFi) extraneous to the underlying medium, any principal component with similar

coefficients (standard deviation/mean < 1) across channels sharing one source optode is regressed out. The six blocks are block averaged to show the flow response.

Participants

19 participants from age 23 to 40 years, with no prior diagnosis or treatment of neurological disorders were recruited for this study. Sex, gender, race, and ethnicity were not considered during recruitment. Participants were recruited through on-campus advertisements including flyers. Of the 19 participants, four showed motion artifacts in intensity time course in more than half the blocks, leaving 15 participants' data for subsequent analysis. The experimental procedure and protocols were approved and carried out in accordance with the regulations of Institutional Review Board of the Boston University. Each participant provided a signed written informed consent form prior to the experiment.

Cap placement

For SCOS human measurements, the same NinjaCap employed for fNIRS measurements is used[50]. The sources and detectors are placed in a NinjaCap, an in-house 3D printed fNIRS cap made of flexible material (NinjaFlex, NinjaTek) with NIRx grommets for compatibility with variable tension spring holders. The cap is placed on the head with respect to EEG 10–10 midline central electrode site (Cz), which is estimated through measurement of nasion, inion, left/right pre-auricular points [51,52]. The cap contains grommet holders arranged in the grid shown in Fig. 1d to ensure the proper placement of optodes. Optodes are placed inside of the grommets and held in place by a variable tension spring holder. A short baseline measurement is taken to confirm that there is a high enough photon flux for effective measurements. If insufficient light is being collected, hair parsing is done to move hair out from the light path to reduce light loss.

Cardiac waveforms measurements

Cardiac signal was recorded for all participants during the same experiments in which they performed the WCS task, as described below. To examine the cardiac waveforms, a few seconds of baseline data was taken before the task began. This also served as an indication of successful cap and optode placement on the head.

Word-Color Stroop task

Participants perform a WCS task containing two conditions (see Fig. 5) based on the task used by Jahani *et al* [34] The stimulus is presented via PsychoPy [53]. For a given trial of the congruent condition, the participant is provided with two-word options and is instructed to select the word which has matching meaning and font color. For a given trial of the incongruent condition, the participant is provided three-word options in a row and a single word prompt below, none of which have self-matching meaning and font color. The participant is instructed to select the word option in the top row which has a meaning that matches the prompt word font color. Participants practice each condition before proceeding to the task. Trial durations are 3 s each, and a block has 6 consecutive trials of either all congruent or all incongruent condition. A run has an initial 20 s rest period followed by 9 blocks of each condition for a total of 18 blocks, the order of which is randomized, with an inter-stimulus rest jittered between 25 to 30 seconds. The total run time is approximately 7 minutes.

Human measurement post-processing

For human measurement, ΔOD and rBFi from short separation (8 mm) SDS channels is linearly regressed out from 19 mm and 33 mm SDS channel signals. The ΔOD and rBFi time series are filtered using a fifth-order Butterworth filter with a cutoff frequency of 0.2 Hz. The filtered data is then block averaged from -2 to 38 seconds with respect to the stimulus onset. This is done for both congruent and incongruent trials resulting in a block averaged activation time course for each trial type and each participant. Systemic physiology and superficial changes are removed using short separation regression. In short separation regression, the zero-meaned short separation channel data is subtracted from the block averaged time course using linear regression. The data is then averaged across all participants to acquire a group averaged result.

Image reconstruction

To reconstruct brain activation from channel space time series, we follow the methods described by Lin et al [44]. In summary, we assume the data can be represented by a linear model:

$$y_{s,d} = A_{s,d} x \tag{10}$$

where $y_{s,d}$, the channel space hemodynamic data, is the product of the underlying brain activation, x, and a sensitivity matrix, $A_{s,d}$, that describes the change observed in channel space given a blood flow perturbation. The sensitivity matrix is estimated using the source and detector green's function acquired by simulating photon propagation through an anatomical head model with a given probe geometry as described in previous works [15,44]. To calculate the decorrelation time dependent green's functions, the absorption term in a traditional photon diffusion simulation is replaced with a decorrelation dependent, correlation absorption term [15,44]:

$$\mu_a = \mu_a + 2\alpha\mu_s' k_0^2 D_b \tau \tag{11}$$

Here μ_a is the absorption coefficient, α is the fraction of dynamic photon scattering events, μ_s' is the reduced scattering coefficient, $k_0^2 = \frac{2\pi n_0}{\lambda}$, D_b is the diffusion coefficient of the brain, and τ is the decorrelation time. We used Monte Carlo simulation with a brain geometry from the cedalion Python module [36]. The simulation is run with 129 logarithmically spaced decorrelation times from 0 s to 4000 µs, the exposure time of the camera. The resulting source and detector green's functions are multiplied to calculate a perturbation term [15,44]. The perturbation is used to calculate a perturbed channel space autocorrelation. The autocorrelation is integrated to calculate the change in contrast from a perturbation in blood flow, thus defining the sensitivity matrix. The product of the inverse of the sensitivity matrix and the channel space data results in the reconstruction of brain activity onto the anatomical model from the simulation:

$$x = A_{s,d}^T (A_{s,d} A_{s,d}^T + \lambda I)^{-1} y_{s,d} \tag{12}$$

Here $A_{s,d}^T$ is the transpose of $A_{s,d}$, I is the identity matrix, and $\lambda = \alpha b$ where $\alpha = 0.05$ is the regularization parameter, and b is the largest eigenvalue of the matrix $A_{s,d} A_{s,d}^T$.

Statistical analysis

Normal distribution across blocks or participants was assumed to calculate standard deviation and standard error for each block or participant averaged data point. For Figs. 5c and 5d, the average of each participant's block-averaged response from 10 to 15 seconds after stimulation and its corresponding standard error were selected to calculate the p-value with the significance level set to $p = 0.05$. The z-score was calculated and then applied to two-tailed cumulative distributive function of normal distribution to obtain the p-value. The mean, standard deviation and standard error are estimated from built-in MATLAB functions.

References

1. Devor, A. *et al.* Coupling of the cortical hemodynamic response to cortical and thalamic neuronal activity. *Proc. Natl. Acad. Sci. U. S. A.* **102**, 3822–3827 (2005).
2. Cheng, X., Sie, E. J., Naufel, S., Boas, D. A. & Marsili, F. Measuring neuronal activity with diffuse correlation spectroscopy: a theoretical investigation. *Neurophotonics* **8**, 035004 (2021).
3. Bandera, E. *et al.* Cerebral Blood Flow Threshold of Ischemic Penumbra and Infarct Core in Acute Ischemic Stroke. *Stroke* vol. 37 1334–1339 Preprint at https://doi.org/10.1161/01.str.0000217418.29609.22 (2006).
4. Leigh, R., Knutsson, L., Zhou, J. & van Zijl, P. C. Imaging the physiological evolution of the ischemic penumbra in acute ischemic stroke. *J. Cereb. Blood Flow Metab.* **38**, 1500–1516 (2018).
5. Bouma, G. J. & Muizelaar, J. P. Cerebral blood flow, cerebral blood volume, and cerebrovascular reactivity after severe head injury. *J. Neurotrauma* **9 Suppl 1**, S333-48 (1992).
6. Cruz Hernández, J. C. *et al.* Neutrophil adhesion in brain capillaries reduces cortical blood flow and impairs memory function in Alzheimer's disease mouse models. *Nat. Neurosci.* **22**, 413–420 (2019).

7. Korte, N., Nortley, R. & Attwell, D. Cerebral blood flow decrease as an early pathological mechanism in Alzheimer's disease. *Acta Neuropathol.* **140**, 793–810 (2020).
8. Globus, M., Mildworf, B. & Melamed, E. Cerebral blood flow and cognitive impairment in Parkinson's disease. *Neurology* **35**, 1135–1139 (1985).
9. Petcharunpaisan, S., Ramalho, J. & Castillo, M. Arterial spin labeling in neuroimaging. *World J. Radiol.* **2**, 384–398 (2010).
10. Grade, M. *et al.* A neuroradiologist's guide to arterial spin labeling MRI in clinical practice. *Neuroradiology* **57**, 1181–1202 (2015).
11. Iutaka, T. *et al.* Arterial spin labeling: Techniques, clinical applications, and interpretation. *Radiographics* **43**, e220088 (2023).
12. Nievelstein, R. A. J. *et al.* Radiation exposure and mortality risk from CT and PET imaging of patients with malignant lymphoma. *Eur. Radiol.* **22**, 1946–1954 (2012).
13. Purkayastha, S. & Sorond, F. Transcranial Doppler ultrasound: technique and application. *Semin. Neurol.* **32**, 411–420 (2012).
14. Carp, S. A., Robinson, M. B. & Franceschini, M. A. Diffuse correlation spectroscopy: current status and future outlook. *Neurophotonics* **10**, 013509 (2023).
15. Boas, D. A., Campbell, L. E. & Yodh, A. G. Scattering and Imaging with Diffusing Temporal Field Correlations. *Phys. Rev. Lett.* **75**, 1855–1858 (1995).
16. Durduran, T., Choe, R., Baker, W. B. & Yodh, A. G. Diffuse Optics for Tissue Monitoring and Tomography. *Rep. Prog. Phys.* **73**, (2010).
17. Sunwoo, J. *et al.* Diffuse correlation spectroscopy blood flow monitoring for intraventricular hemorrhage vulnerability in extremely low gestational age newborns. *Sci. Rep.* **12**, 12798 (2022).

18. Selb, J. *et al.* Prolonged monitoring of cerebral blood flow and autoregulation with diffuse correlation spectroscopy in neurocritical care patients. *Neurophotonics* vol. 5 1 Preprint at https://doi.org/10.1117/1.nph.5.4.045005 (2018).
19. Tellis, G. M., Mesquita, R. C. & Yodh, A. G. Use of diffuse correlation spectroscopy to measure brain blood flow differences during speaking and nonspeaking tasks for fluent speakers and persons who stutter. *Perspect. Fluen. Fluen. Disord.* **21**, 96–106 (2011).
20. Zhou, W. *et al.* Functional interferometric diffusing wave spectroscopy of the human brain. *Sci Adv* **7**, (2021).
21. Robinson, M., Boas, D., Sakadžic, S., Franceschini, M. A. & Carp, S. Interferometric diffuse correlation spectroscopy improves measurements at long source-detector separation and low photon count rate. *J. Biomed. Opt.* **25**, (2020).
22. Bi, R., Dong, J. & Lee, K. Deep tissue flowmetry based on diffuse speckle contrast analysis. *Opt. Lett.* **38**, 1401–1403 (2013).
23. Valdes, C. P. *et al.* Speckle contrast optical spectroscopy, a non-invasive, diffuse optical method for measuring microvascular blood flow in tissue. *Biomed. Opt. Express* **5**, 2769–2784 (2014).
24. Lin, C.-H. P. *et al.* Multi-mode fiber-based speckle contrast optical spectroscopy: analysis of speckle statistics. *Opt. Lett.* **48**, 1427–1430 (2023).
25. Kim, B. *et al.* Measuring human cerebral blood flow and brain function with fiber-based speckle contrast optical spectroscopy system. *Commun. Biol.* **6**, 844 (2023).
26. Huang, Y. X. *et al.* Correlating stroke risk with non-invasive cerebrovascular perfusion dynamics using a portable speckle contrast optical spectroscopy laser device. *Biomed. Opt. Express* **15**, 6083–6097 (2024).

27. Dragojević, T. *et al.* High-density speckle contrast optical tomography of cerebral blood flow response to functional stimuli in the rodent brain. *Neurophotonics* **6**, 045001 (2019).
28. Beslija, F. *et al.* High density speckle contrast optical tomography system for in vivo imaging of deep tissue blood flow. in *Diffuse Optical Spectroscopy and Imaging IX* (eds. Contini, D., Hoshi, Y. & O'Sullivan, T. D.) 126280X (SPIE, 2023).
29. Robinson, M. B. *et al.* Comparing the performance potential of speckle contrast optical spectroscopy and diffuse correlation spectroscopy for cerebral blood flow monitoring using Monte Carlo simulations in realistic head geometries. *Neurophotonics* **11**, 015004 (2024).
30. Zilpelwar, S. *et al.* Model of dynamic speckle evolution for evaluating laser speckle contrast measurements of tissue dynamics. *Biomed. Opt. Express* **13**, 6533 (2022).
31. Cheng, T. Y. *et al.* Choosing a camera and optimizing system parameters for speckle contrast optical spectroscopy. *Sci. Rep.* **14**, 11915 (2024).
32. Varma, H. M., Valdes, C. P., Kristoffersen, A. K., Culver, J. P. & Durduran, T. Speckle contrast optical tomography: A new method for deep tissue three-dimensional tomography of blood flow. *Biomed. Opt. Express* **5**, 1275–1289 (2014).
33. Huang, Y. X. *et al.* Compact and cost-effective laser-powered speckle contrast optical spectroscopy fiber-free device for measuring cerebral blood flow. *J. Biomed. Opt.* **29**, 067001 (2024).
34. Jahani, S., Berivanlou, N. H., Rahimpour, A. & Setarehdan, S. K. Attention level quantification during a modified stroop color word experiment: an fNIRS based study. in *2015 22nd Iranian Conference on Biomedical Engineering (ICBME)* (IEEE, 2015). doi:10.1109/icbme.2015.7404124.

35. Huppert, T. J., Diamond, S. G., Franceschini, M. A. & Boas, D. A. HomER: a review of time-series analysis methods for near-infrared spectroscopy of the brain. *Appl. Opt.* **48**, D280-98 (2009).
36. *Cedalion: FNIRS Analysis Toolbox*. (Github).
37. Fan, C. *et al.* Brain compensatory activation during Stroop task in patients with mild cognitive impairment: a functional near-infrared spectroscopy study. *Front. Aging Neurosci.* **17**, (2025).
38. Ghijsen, M., Rice, T. B., Yang, B., White, S. M. & Tromberg, B. J. Wearable speckle plethysmography (SPG) for characterizing microvascular flow and resistance. *Biomed. Opt. Express* **9**, 3937–3952 (2018).
39. Garrett, A. *et al.* Simultaneous photoplethysmography and blood flow measurements towards the estimation of blood pressure using speckle contrast optical spectroscopy. *Biomed. Opt. Express* **14**, 1594–1607 (2023).
40. Wu, K. C. *et al.* Enhancing diffuse correlation spectroscopy pulsatile cerebral blood flow signal with near-infrared spectroscopy photoplethysmography. *Neurophotonics* **10**, 035008 (2023).
41. Urner, T. M. *et al.* Normative cerebral microvascular blood flow waveform morphology assessed with diffuse correlation spectroscopy. *Biomed. Opt. Express* **14**, 3635–3653 (2023).
42. Wu, M. M. *et al.* Complete head cerebral sensitivity mapping for diffuse correlation spectroscopy using subject-specific magnetic resonance imaging models. *Biomed. Opt. Express* **13**, 1131–1151 (2022).
43. Boas, D. A. *et al.* Establishing the diffuse correlation spectroscopy signal relationship with blood flow. *Neurophotonics* **3**, 031412 (2016).

44. Lin, C.-H. P. *et al.* Anatomical modeling and optimization of speckle contrast optical tomography. *bioRxivorg* (2023) doi:10.1101/2023.09.06.556565.

45. Markow, Z. E. *et al.* Ultra-high density imaging arrays for diffuse optical tomography of human brain improve resolution, signal-to-noise, and information decoding. *bioRxivorg* (2023) doi:10.1101/2023.07.21.549920.

46. Selb, J. *et al.* Effect of motion artifacts and their correction on near-infrared spectroscopy oscillation data: a study in healthy subjects and stroke patients. *J. Biomed. Opt.* **20**, 56011 (2015).

47. Poon, C., Rinehart, B., Li, J. & Sunar, U. Cerebral blood flow-based resting state functional connectivity of the human brain using optical diffuse correlation spectroscopy. *J. Vis. Exp.* (2020) doi:10.3791/60765.

48. Gao, Y. *et al.* Short-separation regression incorporated diffuse optical tomography image reconstruction modeling for high-density functional near-infrared spectroscopy. *Neurophotonics* **10**, 025007 (2023).

49. Tucker, S. *et al.* Introduction to the shared near infrared spectroscopy format. *Neurophotonics* **10**, 013507 (2023).

50. von Lühmann, A. *et al.* ninjaCap: a fully customizable and 3D printable headgear for functional near-infrared spectroscopy and electroencephalography brain imaging. *Neurophotonics* **11**, 036601 (2024).

51. Klem, G. H., Lüders, H. O., Jasper, H. H. & Elger, C. The ten-twenty electrode system of the International Federation. The International Federation of Clinical Neurophysiology. *Electroencephalogr. Clin. Neurophysiol. Suppl.* **52**, 3–6 (1999).

52. von Lühmann, A. *et al.* ninjaCap: A fully customizable and 3D printable headgear for fNIRS and EEG brain imaging. *bioRxiv* (2024) doi:10.1101/2024.05.14.594159.

53. Peirce, J. W. Generating stimuli for neuroscience using PsychoPy. *Front. Neuroinform.* **2**, 10 (2008).

Acknowledgments
We thank Joseph O'Brien, De'Ja Rogers, Sudan Duwadi, Sreekanth Kura, Bingxue Liu, Allen Zhou, Lina Lin, Kyle Bohl, Matthew Simkulet, Zahid Yaqoob, and John T. Giblin for useful discussions. This project is supported by NIH UG3EB034710 (Cheng), NIH R01NS135081 (Franceschini), and NIH T32-NS136080.

Funding:
National Institutes of Health grant UG3EB034710 (XC, DAB)
National Institutes of Health grant R01NS135081 (MAF)
National Institutes of Health grant T32-NS136080 (DAB)

Author contributions:
Conceptualization: BK, DAB, and XC
Methodology: BK, ACH, EH, BBZ, M.Robinson, M.Renna, LC, SC, SAC, MAF, DAB, and XC
Investigation: BK, ACH, TYC, JEA, MAY, and XC
Visualization: BK, ACH, LC, DAB, XC
Supervision: MAF, DAB, XC
Writing—original draft: BK, ACH, XC
Writing—review & editing: BK, ACH, TYC, JEA, BBZ, MAY, SAC, MAF, DAB, XC

Competing interests: The authors declare no competing interests.

Data and materials availability: Data used to generate the main and supplementary figures are available on Figshare database. All other datasets that support the findings of this study are available from the corresponding author upon reasonable request. **The links will be provided before the manuscript is published.**

Code availability: The SCOS control board code is written in C++ and available on GitHub. The camera acquisition code is written in Python and available on GitHub. The SCOS preprocessing and data analysis pipeline is written in MATLAB and available on GitHub. Image reconstruction is written in Python and available on GitHub. All code has been deposited Zenodo. Any other code including those used to generate the manuscript's figures are available from the corresponding author on reasonable request. **These links will be provided before the manuscript is published.**

Figures and Tables

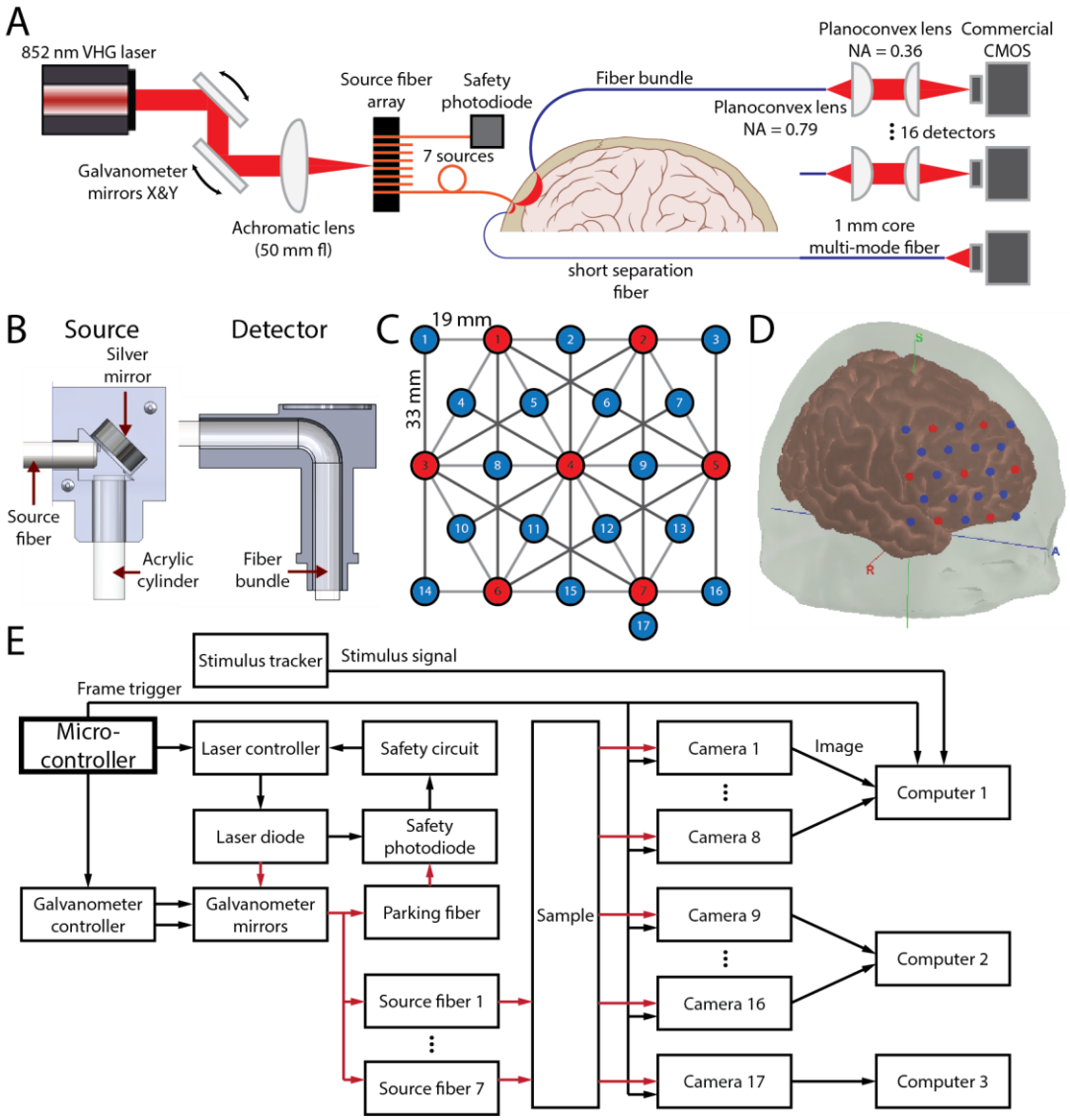

Fig. 1. Multi-channel SCOS system setup. (**A**) Schematic of the multi-channel SCOS system. (**B**) Cross section CAD diagram of the source fiber holder (left) and detector fiber holder (right). (**C**) 76 x 66 mm grid array consisting of 7 sources (red) and 17 detectors (blue). The 17th detector has a SDS of 8 mm from source #7. (**D**) The location of the source detector grid array on the head for the cognitive task. (**E**) Information flow diagram of the SCOS control system. Black arrows indicate electrical signal while red arrows indicate optical signal.

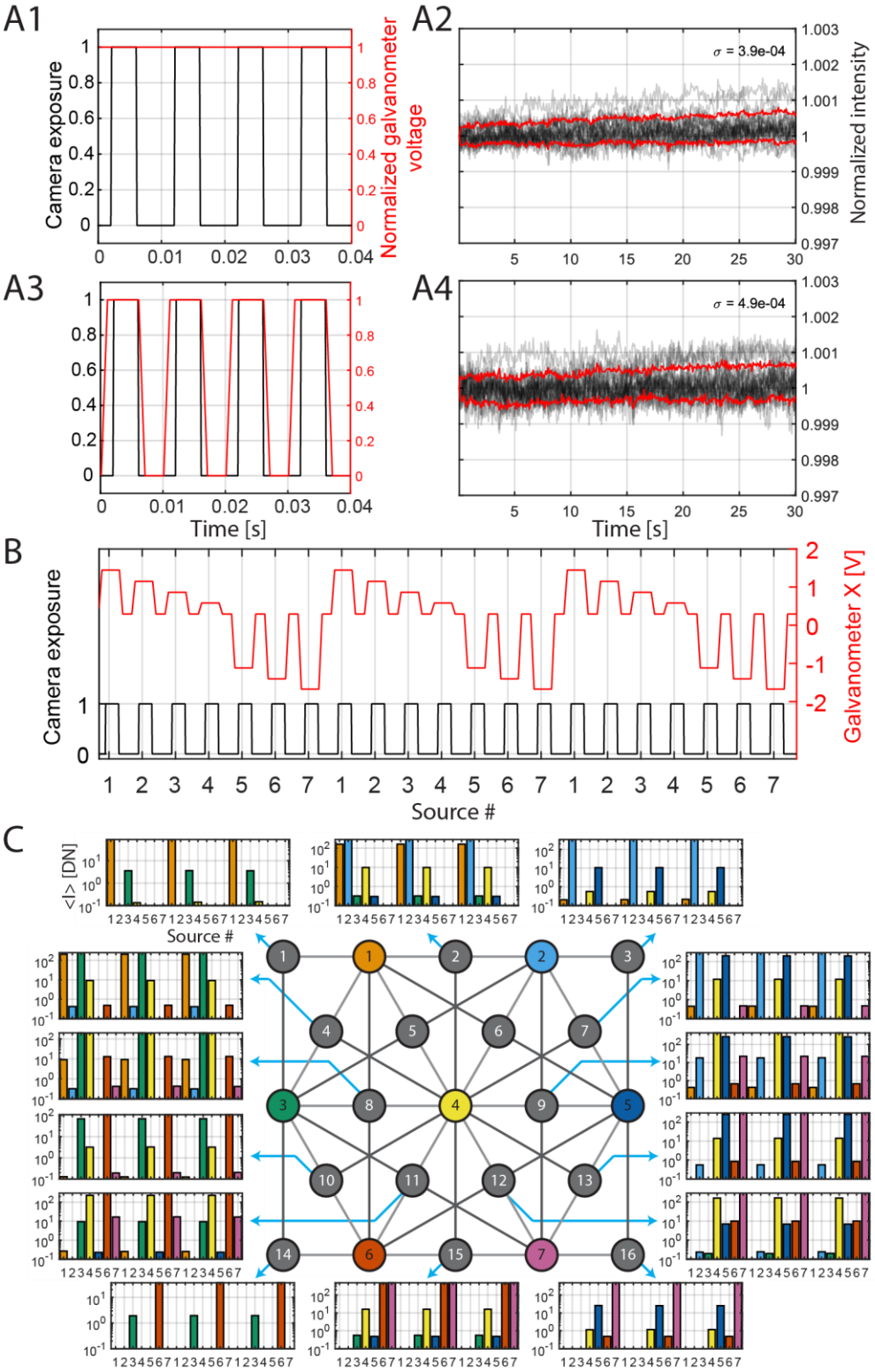

Fig. 2. Temporal multiplexing scheme of the sources. (**A**) Intensity stability with and without galvanometer mirror movement. The time course for the source (red) and detector (black) controls when the galvanometer mirror is not moving (A1) and moving with a trapezoidal form (A3). (A2) and (A4) each present 20 of 30 second time courses

normalized to first value for (A1) and (A3) galvanometer movement respectively. The solid red lines describe the ±1 standard deviation from mean time course. (**B**) Example synchronized camera exposure and galvanometer voltage time course. (**C**) The intensity time course measured at most (14) of the detectors using a liquid phantom sample when the 7 sources are illuminated sequentially.

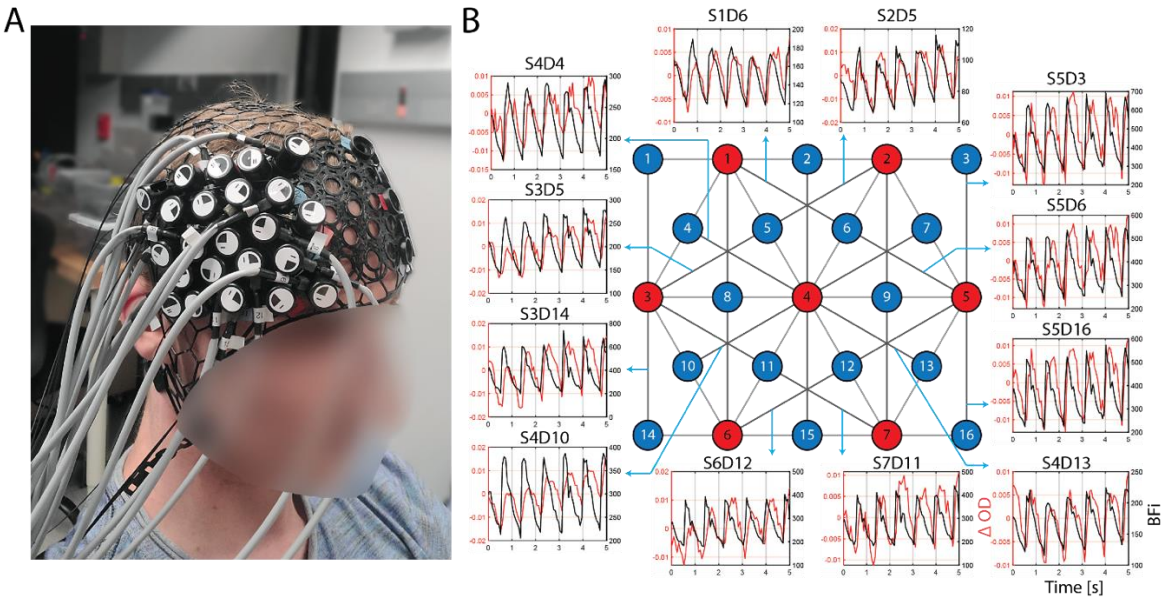

Fig. 3: Cardiac waveforms measured in 33 mm SDS channels. (**A**) An author wearing the multi-channel SCOS system on the right forehead. (**B**) Cardiac signal in ΔOD (red) and BFi (black) shown from multiple 33 mm SDS channels.

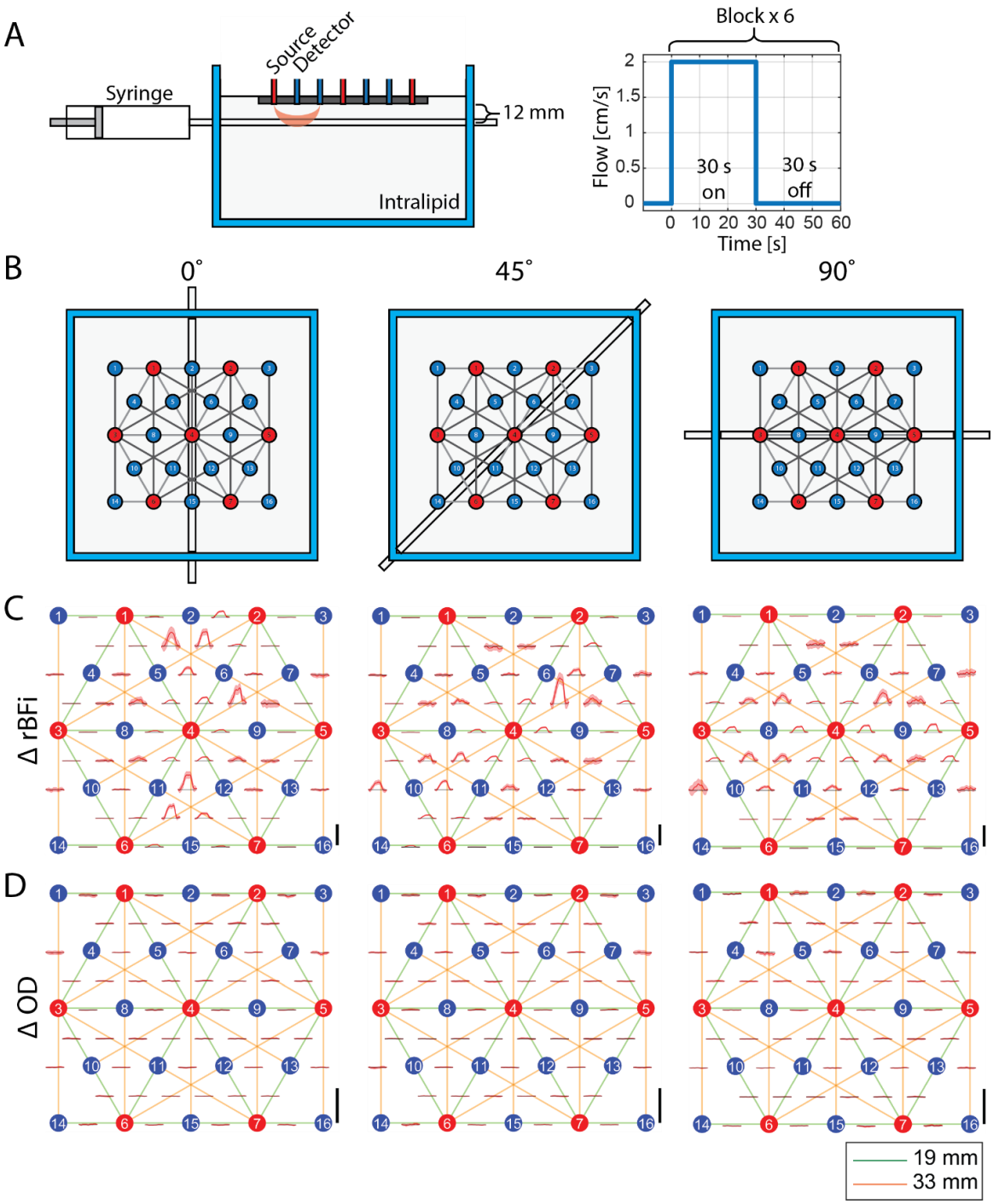

Fig. 4. Measurement of spatially specific flow changes in dynamic phantom. (**A**) Dynamic phantom flow measurement setup, and the time courses of the flow within the tube. (**B**) The orientations of the source-detector layout relative to the tube at 0° (left), 45° (middle), and 90° (right). (**C**)-(**D**) ΔrBFi (C) and ΔOD (D) Time course signals averaged over 6 blocks for the 19 mm and 33 mm SDS channels, shown in the plot-probe profile using the Homer 3 software. Shaded area is the standard error of the time course over the blocks. The y-scale shown as black vertical bar on the right-most plots represents 20% for ΔrBFi and 0.02 for ΔOD respectively.

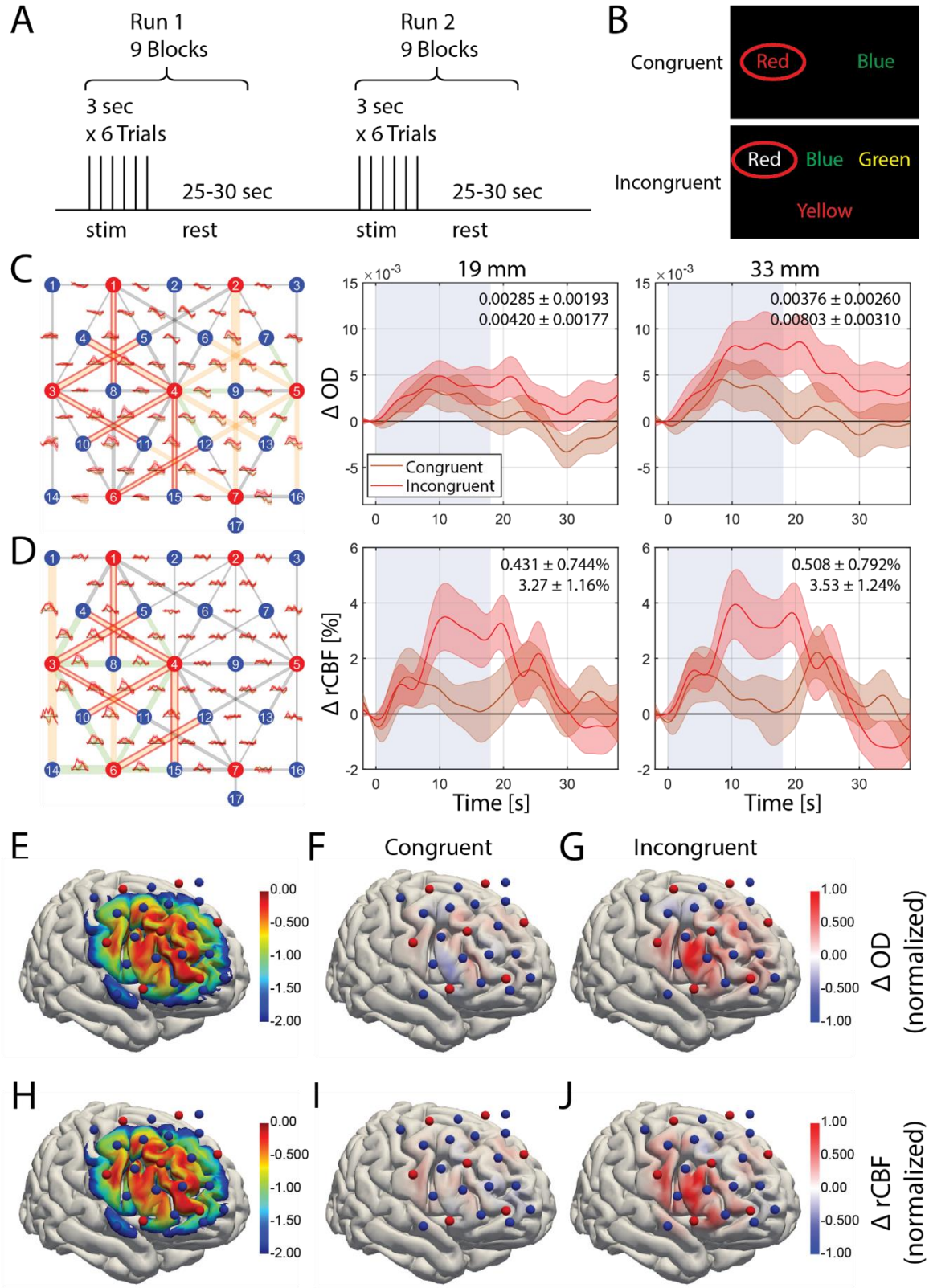

Fig. 5. Task based human brain activation measurement using the multi-channel SCOS system. (**A**) Illustration of the task. Each participant has 2 runs consisting of 9

blocks each, and each block is composed of 6 WCS task trials each lasting 3 seconds, followed by a rest time of 25-30 seconds. (**B**) Demonstration of the congruent (left) and incongruent (right) WCS task. (**C**) Channel space ΔOD map. 19 mm SDS channels (green) and 33 mm SDS channels (orange) with significant ΔOD activation (mean > 1.96 standard error), as well as block and channel averaged ΔOD time course for each SDS. (**D**) Channel space ΔrCBF map. (**E**) Normalized sensitivity map for ΔOD, normalized, log10 scale. (**F,G**) WCS induced ΔOD (t > 10s & t < 15s) reconstructed image for congruent (F) and incongruent (G) tasks. (**H**) Normalized sensitivity map for ΔrCBF, normalized, log10 scale. (**I,J**) WCS induced ΔrCBF (t > 10s & t < 15s) reconstructed image for congruent (F) and incongruent (G) tasks.